### Title
Revealing Molecular Mechanisms in Hierarchical Nanoporous Carbon via Nuclear Magnetic Resonance




### Journal
Matter, 3(6)

### ISSN
2590-2393



### Authors
Mao, Haiyan
Tang, Jing
Xu, Jun
et al.



### Publication Date
2020-12-01

### DOI
10.1016/j.matt.2020.09.024

Peer reviewed

# Revealing Molecular Mechanisms in Hierarchical Nanoporous Carbon by Nuclear Magnetic Resonance

Haiyan Mao[1†], Jing Tang[2,7†], Jun Xu[1], Yucan Peng[2], Jun Chen[2], Bing Wu[1], Yuanwen Jiang[4], Kaipeng Hou[3], Shuo Chen[5], Jiangyan Wang[2], Hye Ryoung Lee[2], David M. Halat[1,6], Bing Zhang[3], Wei Chen[2], Ariel Z Plantz[1], Zhiyi Lu[2], Yi Cui[2,7*] and Jeffrey A. Reimer[1,6*]

[1]Department of Chemical and Biomolecular Engineering, University of California, Berkeley, California, 94720, USA.

[2]Department of Materials Science and Engineering, Stanford University, Stanford, California, 94305, USA.

[3]Department of Chemistry, University of California, Berkeley, California, 94720, USA.

[4]Department of Chemical Engineering, Stanford University, Stanford, California, 94305, USA.

[5]Department of Physics, University of California, Berkeley, California, 94720, USA.

[6]Materials Science Division, Lawrence Berkeley Laboratory, Berkeley, California, 94720, USA.

[7]Stanford Institute for Materials and Energy Sciences, SLAC National Accelerator Laboratory, 2575 Sand Hill Road, Menlo Park, California, 94025, USA.

† Haiyan Mao and Jing Tang contributed equally to this work

*Correspondence and requests for materials should be addressed to **Yi Cui (yicui@stanford.edu) (Y.C.); Jeffrey A. Reimer reimer@berkeley.edu (J.A.R.)**.

## Summary

Hierarchical nanoporous carbons (HNC) have been proven to be an effective, sustainable and efficient adsorbent for the adsorption of volatile organic compounds (VOCs) and $CO_2$, although questions remain regarding the hierarchical structure regulation, and the adsorption mechanisms of adsorbate uptake and interactions within the HNC. Herein, we synthesize a honeycomb structured HNC from wood using a microwave-induced heating method incorporating $K_2CO_3$ activation. There materials are shown to exhibit Murray's Law multi-scale structures with micro- and mesopores, prompting a molecular scale study of adsorbate adsorption using nuclear magnetic resonance (NMR). NMR chemical shifts are consistent with ring current effects from the adsorbent, and integrated intensities are readily converted to mass-of-adsorbate per mass-of-adsorbent, providing a convenient and fast way to quantitate adsorption of adsorbate in HNC. Vapor phase VOCs adsorption results show NMR chemical shift changes with time after adsorption, suggesting initial adsorption into mesopores, followed by diffusion into micropores with increasing adsorption time. Persistent differences in observed shifts for adsorbed liquid vis-à-vis vapor phase in these HNC demonstrate of Schroeder's Paradox. These HNC also show high $CO_2$ adsorption capacity (4.3 mmol $g^{-1}$ at 298 K and 1 bar) portending applications to carbon capture.

## Introduction

Volatile organic compounds (VOCs) are common air pollutants contributing to the formation of ground-level ozone and carcinogens, known to be harmful to human health[1]. Carbon dioxide ($CO_2$) is the primary anthropogenic source of greenhouse gases that has impacted the earth's biosphere, especially climate change[2]. The rational design of renewable, multidimensional and microscopic materials for the adsorption of VOCs and $CO_2$ is therefore an important objective in functional materials research[1,3,4]. In particular, porous materials with nanosized pores play important roles in the science and technology of VOCs and $CO_2$ adsorption and separation[5,6].Nanoporous carbons derived from biomass are particularly promising due to their cost-efficient scalable fabrication, sustainable sourcing, high surface area and microporous dominated structure[7,8,9]. Typically, adsorption in such nanoporous carbon is determined by physical adsorption (via van der Waals forces) and ultimately micropore filling and capillary condensation[10,11]. Mesopores play an important role by providing transport channels for the adsorption and desorption of molecules, as well as further adsorption sites[12,13]. We therefore focus our attention on VOC and $CO_2$ adsorption within sustainable manufacturable[14] and hierarchically structured nanoporous carbons that exhibit a panoply of pore sizes.

Various synthetic methods have been proposed and developed for hierarchically nanoporous carbons (HNC), but many methods suffer from lack of structural control, harsh synthesis conditions, poorly degrading scaffolds and unsuitable pores (e.g. clogged pores and beaded holes)[15,16,17,18]. Inspired by plant structures, so-called Murray's Law materials have garnered attention recently owing to the ability to regulate pore diameters from macroscopic to microscopic dimentions[19,20]. Nevertheless, progress in synthesizing Murray's Law materials remains slow, hindered by the ever-present bottleneck issues within the interconnected pores. Herein we synthesize HNC derived from pinewood that follows Murray's Law of interconnected micro- and mesopores using an innovative microwave-induced method incorporating $K_2CO_3$ activation[21,22] (**Figure 1a**).

Several characterization methods have been used to investigate the adsorption performance of HNC, such as adsorption capacity measurements via breakthrough experiments and gas adsorption isotherms[23,24,25,26]. The interactions between adsorbed molecules and the carbon pores are important factors during adsorption process and cannot be revealed by bulk methods[27]. Solid-state nuclear magnetic resonance (SSNMR), however, is well suited to probe both local microscopic structure and the dynamical properties of guest compounds confined in hierarchical porous carbons[28,29]. To date, NMR has been utilized to probe the environment of adsorbed molecules onto host porous carbon-based materials[26] with applications to supercapacitors[29,30], adsorption[30], and hydrogen storage[31]materials. These studies led us to investigate hierarchical carbon materials by employing a combination of proton NMR and adsorption isotherm measurements.

We compare solid-state NMR studies of three typical liquid and gaseous VOCs adsorbates: acetone, toluene and *n*-hexane, as well as carbon dioxide. These molecules were chosen because they are representative of environmental adsorption technologies and each molecule possesses different dimensions and polarity. We observe that the adsorption of the VOCs from the liquid phase reflects uptake into the mesopores of the hierarchical nanoporous carbons; in all adsorbates the resulting chemicals shifts show the effects of polyaromatic ring currents from the carbon adsorbent. Integrating the

NMR signals from liquid-adsorbed VOCs yields uptakes of VOC mass that compare favorably to those determined by adsorption experiments. We found that the observed NMR chemical shifts of VOCs obtained by gas-phase and liquid-phase exposure are not the same, an apparent manifestation of Schroeder's Paradox[32]. Finally, carbon dioxide physisorbs into HNC with a surprising capacity. Together, these findings offered detailed insights into the interactions between liquid/gaseous adsorbates and hierarchical nanoporous carbons via NMR.

## Results and Discussion

## Physicochemical and structural characteristics

The argon adsorption-desorption isotherm at 77 K of HNC is demonstrated in **Figure 1b**, and **Table S1**. After microwave heating and $K_2CO_3$ activation, we observe that at relative pressure ($P/P_0$) below 0.05, the nitrogen uptake increases sharply with the increase in relative pressure, proving the existence of micropore structure. These adsorption isotherms are close to type a I-IV hybrid shape as defined by the BBDT classification[33].

The specific surface area BET and total pore volume of our HNC after the $K_2CO_3$/microwave treatment were remarkably improved (**Table S1**). The micropore surface area and volume significantly increased from 30 to 1857 $m^2/g$, with the micropore volume of biochar increasing from 0.016 to 0.741 cc/g, indicating that the micropores were developed in the mesopore walls while some mesoporous channels collapse. The development of porosity is associated with the reaction of $K_2CO_3$ and C leading to the formation of $K_2O$, K, CO, and $CO_2$ where the high microwave temperature is assumed to accelerate the activation reaction[34]. The potassium species formed during the activation step diffuse into the internal structure of the biochar matrix, which is presumed to widen existing pores as well as to create new ones. Consequently, the presence of $K_2CO_3$ promotes the formation of dominant micropores and a small fraction of mesopores, a much larger surface area, as well as a larger pore volume. The measured surface areas are 3.4 times higher than those of carbons activated by $K_2CO_3$ via thermal heating of samples derived from tobacco stem[35].

The pore size distribution curves plotted in **Figure 1c** are derived from argon adsorption measurements using the Horváth-Kawazoe method[36] and indicate that the HNC manifest a wide pore size distribution covering micropores (0.65-2 nm) and mesopores (2-50 nm). The overwhelming majority of pore sizes include micropores (<2 nm), even supermicropores (0.7-2 nm) and even ultramicropores (<0.7 nm). Argon adsorption-desorption isotherms (**Figure 1c**) reveal a micropore distribution with a mean size of 0.8 nm ($D_{micro}$); micropores within the HNC are elucidated via the low relative pressure region. The $K_2CO_3$/microwave activated HNC thus appears to obey Murray's Law with three layers of structure at the micro-/mesopore level as well as abundant interconnected pores. Such a super hierarchical pore structure aids in the diffusion of adsorbates and is helpful to enhance the adsorption and desorption performance of the HNC.

Transmission electron microscopy (TEM) image (**Figure 1d**) shows a disordered hierarchical nanoporous structure containing mesopores. The large quantities of white spots between the disordered carbon layers suggests that abundant mesopores exist in the hierarchical carbon from pinewood. To observe wormhole-like pores as well as the interconnectivity of micropores and mesopores more clearly, the real space images were transformed by an auto-threshold function to binary images (**Figure S1**). The transformed image reveals that the micropores and mesopores are interconnected. Representative scanning electron microscopes (SEM) image of HNC is depicted in **Figure 1e**, where notably the perfect honeycomb structure and typically prismatic rectangular cells from the natural pinewood appear to be maintained after chemical activation. These dimensions of the cells were ca. 20 μm and the wall thickness was ca. 2 μm. It is important to note that there was no evidence of rupture of the pinewood pore walls, indicating that the wall material had a high tensile strength such that $K_2CO_3$ could be impregnated and dissolved $K_2CO_3$ could be removed. Upon $K_2CO_3$/microwave activation, the pores were etched and developed during the reaction of K with carbon. These results are similar to previously published SEM images of carbonized and activated virgin cork[37,38]. The present $K_2CO_3$/microwave activation of pinewood yields an interconnected HNC obeying Murray's Law via a facile, low-cost, and environmentally friendly process.

## Adsorption of liquid acetone in hierarchical nanoporous carbon

Proton ($^1H$) spin-echo magic angle spinning (MAS) NMR spectra of acetone adsorbed onto hierarchical nanoporous carbon for the range 23 wt % to 100 wt % loadings are shown in **Figure 2a**. Initial adsorption gives rise to a broad signal at -2.5 ppm, shifted to low frequency from that for liquid acetone (2.2 ppm) by 4.7 ppm, which is assigned to the "in-pore" acetone (**Figure 2b**). This shift to lower frequency results from ring currents emanating from the aromatic rings of the graphene planes in the pore walls[39]. This has previously been confirmed experimentally and theoretically on microporous/mesoporous porous carbon[39].

The ring current effect is strongly dependent on the distance between the NMR-observed nucleus and the center of the aromatic ring[40,41].

With the increase of acetone loading, the broad line grows in intensity until it reaches a plateau at higher loadings (63 wt %), suggesting pore-filling and saturation. As the loading level increases further to 82 wt %, a narrower peak appears at 2.1 ppm, a shift that is close to that of the methyl protons in neat acetone. The peak is associated with liquid acetone external to the HNC pores, which is assigned to the "ex-pore" acetone (**Figure 2b**). The chemical shift deviation between the in-pore resonance and neat acetone is quantified by $\Delta\delta=\delta_{¿-pore}-\delta_{neat}$, and has a value of -4.5 ppm here (corresponding to the two peaks in **Figure 2a**).

To quantitate exchange between the in-pore and ex-pore enviroments[41], two-dimensional $^1H$ homonuclear exchange experiments[42] were conducted at various mixing times (0.001, 0.1 and 0.25 s); the results are shown in **Figure 2c to 2e**. As expected, the cross peaks appearing at mixing times in excess of 0.1 s confirm that acetone exhibits slow exchange between "in-pore" and "ex-pore" environments.

## Adsorption of liquid toluene and *n*-hexane in hierarchical nanoporous carbons

The $^1H$ spin echo-MAS spectra of toluene and *n*-hexane adsorbed onto HNC as a function of loading are in **Figure S2**. The qualitative features of these spectra are analogous to those observed from acetone; the methyl and aromatic proton resonances from toluene reveal in-pore and ex-pore environments, as do the $CH_3$ and $CH_2$ resonances from *n*-hexane. At a mass ratio of 62 wt % the pores of HNC become "full" and the toluene/*n*-hexane loading reaches saturation. As the loading increases further the narrow lines emanating from ex-pore features become prominent. Therefore, the four peaks at low and high frequencies are assigned to in- and ex-pore toluene respectively (**Figure S2a**). For these adsorbates, we calculate Δδ to be -4.2 ppm (acetone), -4.2 ppm (toluene) and -4.4 ppm (both $CH_3$ and $CH_2$ resonances from *n*-hexane (**Figure S2b**). The chemical shift deviations Δδ are very similar for the three adsorbates, indicating that the underlying mechanism is mainly due to ring-current shifts associated with the aromatic rings in the HNC.

## Comparison of uptakes between NMR spectra and adsorption isotherms

Quantitative NMR spectroscopy can be used to provide an alternative method for obtaining adsorption uptakes[43]. The adsorption isotherms of acetone/toluene/*n*-hexane for our HNC were acquired using a sorption analyzer at 298 K with $N_2$ as the carrier gas and are shown in **Figure 3c**. Proton ($^1$H) single-pulse NMR spectra of liquid acetone, toluene and *n*-hexane spectra adsorbed at various loadings were deconvoluted and integrated using the DMFit software[44] (**Figure S3**), thereby providing the amount in mmol of adsorbed in-pore VOC per gram of HNC (**Figure 3c**). To compare NMR uptake to gas sorption studies, the abscissa is given as mmol of VOC adsorbed: for the NMR data this is the amount of liquid VOC placed into the sample, and for the isotherm data this is determined by converting the partial pressure ($P/P_0$) to mmol via the Peng–Robinson equation of state[45]. The result shows that ultimate uptake of adsorbates as measured from adsorption isotherms are in good agreement with those determined from the NMR spectra. The reason for the lag at low uptakes is unclear and requires further studies.

The adsorption capacity of the three compounds within the HNC was found to be in the order of toluene > acetone > *n*-hexane. This order of adsorption capacity clearly demonstrates the effects of molecular dimension and polarity of these three VOCs[41,46]. By way of comparison with the HNC synthesized in this work, VOC isotherms and adsorbate capacity on commercial activated carbon were also performed. Our HNC exhibit higher adsorption capacities for all VOCs compared with commercial activated carbon (**Figure S4**). The saturated toluene, acetone and *n*-hexane adsorption capacities reached 11.9, 8.8 and 6.8 mmol/g, respectively, which are 1.5, 1.6 and 1.9 times higher than those of commercial activated carbon, respectively. Consequently, our HNC that demonstrates a high adsorptive performance of VOCs provides a cost-effective alternative to commercial activated carbon in many air quality remediation and treatment applications.

## VOCs vapor adsorption in hierarchical nanoporous carbons

In many practical applications, VOC adsorption occurs from the vapor phase rather than the liquid phase where the time required for adsorbents to equilibrate with dosed gas has significance for process swing designs. Therefore, we have further examined vapor VOCs loaded onto HNC as a function of adsorption time. **Figure 4b** depicts the $^1$H NMR spectra of acetone vapor adsorbed onto HNC as a function of adsorption time at room temperature. After exposure to acetone vapor (**Figure 4b**) for 1 min, a broad peak at -0.4 ppm (labeled "A") is observed. With increasing adsorption time to 91 min, the intensity of peak "A" gradually decreases and shifts upfield, ultimately disappearing after 150 minutes. A second, upfield peak a (~2.5 ppm, "peak B") increases in intensity to a maximum intensity, suggesting of saturation of the micropores. **Figure 4g** further confirms the total proton NMR signal integrated from the "within pore" environments (both peak A and peak B) changes as a function of adsorption time where, as expected, the adsorption uptake increases with time and reaches saturation at ~91 min. Compared to the liquid-phase loaded HNC spectrum (**Figure 4a**), the ex-pore peak at ~2 ppm does not appear, indicating that all the gas molecules enter into the pores and no extra molecules remain exterior to the pores.

Noting that adsorbate molecules in smaller pores experience a greater average degree of ring current shielding and thus demonstrate a greater shift to low frequency than those in larger pores[30], the more negative chemical shift for peak B suggests that these acetone molecules are adsorbed in smaller pores vis-á-vis those corresponding to peak A. We consider two hypotheses to explain the NMR spectra shown in **Figure 4c to 4g**. First, diffusion of acetone within the HNC pore network over time could change the observed NMR shifts as the adsorbate molecules diffuse to differing carbon-pore environments (**Figure 4c**). To test this hypothesis, we performed a $^{1}H$ NMR experiment where acetone vapor was exposed to HNC for 1 minute, and then a further 3 hours of exposure to $N_2$ gas for diffusion/equilibration. **Figure S5** shows that the chemical shift of the spectrum is not changed after waiting for 3 hours. Additionally, we conducted a $^{1}H$ NMR experiment where acetone vapor was exposed to HNC for 1 minute, followed by heating the acetone- adsorbed samples to 55 ℃ for 30 min and then cooling down to room temperature. **Figure S6** shows that the chemical shift of the spectrum is unchanged after the treatment. Therefore, the changes in **Figure 4b** are unlikely to be due to the acetone diffusion over time within the HNC.

A second hypothesis is that thermodynamic effects are responsible for the observed NMR behavior. Schroeder's Paradox[32], wherein adsorption of saturated vapor differs from that when exposed to liquid, has been reported and discussed extensively in the literature[47,48]. Schroeder's Paradox occurs in strongly interacting systems, in which the materials undergo a high degree of swelling[48]. The data shown in **Figure 4b** suggest that the distribution of acetone in HNC mesopores depends upon the way in which the adsorbate was introduced, and that neither time nor modest temperature annealing redistribute the adsorbed acetone molecules so as to yield the same molecular environments. **Figure 4d-4g** interpret the manifestation of Schroeder's Paradox in the aspect of differences in chemical shifts **(Figure 4e)** and adsorption capacities (Figure 4f and 4g) for liquid and gaseous acetone. **Table S3** displays spectral simulation parameters of Gaussian/Lorentzian of liquid and vapor VOCs obtained from deconvolution using the DMfit software. We summarize the adsorption capacities of HNC for all VOCs after liquid and vapor exposure in **Table S4**. It is clear that the adsorption capacity of saturated VOCs within the HNC is quite different between saturated liquid and vapor VOC; for example, the adsorption capacity of 11.8 mmol/g for acetone vapor with exposure time of 150 min is quite different from that of liquid acetone with 8.8 mmol/g at 141 wt % loading (**Figure 4f and 4g**). This difference of adsorption capacities would seem to be an *adsorbate-probed* manifestation of Schroeder's Paradox.

The observed chemical shifts of adsorbed acetone from the liquid phase are different from those arising from vapor-phase adsorbed acetone (**Figure 4e**). This might be rationalized assuming that the acetone vapor diffuses into the pore structure in a different way than that of liquid acetone. A comparison of effective liquid and vapor diffusion time (**Figure 2a and Figure 4b**) in HNC reveals that acetone vapor requires a longer period (150 min) to diffuse from mesopores to reside in microporous environments, as confirmed by the large nucleus-independent chemical shifts (NICS) value obtained at that time. After 16 minutes, two peaks are clearly present, revealing that mesopores and micropores are filled with acetone molecules, which do not undergo exchange on the NMR time scale, thus indicating that slow diffusion in HNC (**Figure 2c to 2e**). However, liquid acetone diffuses immediately into the micropores (**Figure 2a, 23**

**wt %**) and fills the mesopores at higher loading (**Figure 2a, 63 wt %**), in addition to causing spectral broadening spectra at -2.5 ppm (**Figure 4e**), emphasizing that limited diffusion occurs on the NMR time scales.

**Figure 5b** presents the $^1H$ NMR spectra of HNC subjected to vapor-phase toluene as a function of adsorption time. After toluene exposure for 1 min, several peaks appear. Those with the largest shifts are easily assigned to ex-pore aromatic and ex-pore methyl protons owing to the similarity of their shifts to those of neat toluene, consistent with a picture in which some toluene molecules are not able to go into the pores after short exposure times because the molecular size of toluene is larger than that of the narrow pores in the HNC. Assignment of the upfield shifts proton peaks is not clear, yet the shifts suggest ring current effects and thus we assign them to in-mesopore (C-H) and in-mesopore $CH_3$, as indicated in **Figure 5b** (the spectrum at 1 min). With an increase in adsorption time (150 minutes) the two broad peaks at 1.28 and -0.68 ppm shift further upfield (i.e., lower chemical shift values) to -2.74 and -3.85 ppm. Again, the increased ring current effects are the likely cause, and thus we assign these peaks to the in-micropore (C-H) and in-micropore ($CH_3$), respectively. Interestingly, for the spectrum of vapor adsorbed HNC at 150 min, the signal at 0.88 ppm assigned to in-mesopore (C-H) environments does not move to lower chemical shift, indicating that there are toluene molecules still adsorbed in the mesopore due to the larger molecule size of toluene, as compared to the narrow pore size of HNC. Compared to the liquid adsorption spectrum at 100 wt % toluene (**Figure 5a** on the top), the vapor spectra provide more subtle information about the interactions in different pores as a function of adsorption time. As in the case of acetone, it would appear that Schroeder's Paradox is at play.

The $^{1}H$ NMR spectra obtained for vapor *n*-hexane vapor within the HNC as a function of adsorption time are shown in **Figure 5d**. With the initial exposure to *n*-hexane for 1 min, $^{1}H$ MAS NMR signals of the in-mesopore ($CH_2$) and in-mesopore ($CH_3$) molecules in the range of ~2 to ~-2 ppm overlap, while the broad peak at -3.94 ppm emerges and is assigned to the in-micropore ($CH_2$ and $CH_3$) environments. At 6 min, the sharp peak at 1.98 pm is assigned to the overlaps of two environments corresponding to ex-pore ($CH_2$) and ex-pore ($CH_3$). With increasing of adsorption time, as expected, in-mesopore ($CH_2$) and in-mesopore ($CH_3$) signals diminish, while those at -3.71 ppm attributed to the in-micropore ($CH_2$ and $CH_3$) increase. It is interesting to note that the chemical shift difference ($\Delta\delta = 0.6$ ppm) between ex-pore *n*-hexane vapor and ex-pore liquid *n*-hexane peaks (**Figure 5c**) is probably due to a small amount of chemical exchange between the ex-pore and in-pore gas species, which shifts the chemical shift of the vapor ex-pore vapor away from the liquid ex-pore[31]. As also observed with acetone and toluene, the nature of pore occupancy by the adsorbate depends on whether the sample is exposed to saturated vapor or liquid.

## $CO_2$ capture performance

**Figure 6a** shows the $CO_2$ adsorption isotherms for HNC at 298 K and 1 bar. Remarkably, it can be found that our HNC exhibited a high $CO_2$ adsorption capacity of 4.3 mmol $g^{-1}$, thereby reflecting a strongly competitive $CO_2$ adsorption capacity among the other porous framework materials (e.g., 3.78 mmol $g^{-1}$ for rice husk derived activated carbons at 298 K and 1 bar[49]; for comparison the capacity of MOF-74 at 298 K and 1 bar[50] is 4.1 mmol $g^{-1}$). The $^{13}C$ MAS NMR spectra of $^{13}CO_2$-dosed HNC exhibit resonances which were assigned to physisorbed $CO_2$ at 121.7 ppm (**Figure 6c**). A similar peak at 124.7

ppm was observed in MOF-274[44]. The -6 ppm chemical shift vis-à-vis free gas-phase $CO_2$ (127.7 ppm at 1 bar) is due to aromatic ring currents[51]. Thereby, our HNC has excellent $CO_2$ capacity that, combined with the low-cost, sustainable, facile and up-scalable synthesis method warrants further study with potential application towards carbon capture technologies.

## Conclusions

In summary, we prepared hierarchical nanoporous carbons from pinewood that exhibits multi-branching micro-and-mesopores and obeys Murray's Law. These HNC exhibit a large surface area (2765 $m^2/g$) and micropore volume (0.741 cc/g), which portends a potentially important role in the adsorption of gases. We probed the adsorption of VOCs at the molecular level via $^1H$ MAS NMR. Acetone, toluene and *n*-hexane were found to exhibit NMR spectra that quantify the mass of adsorbate, and changes of the spectra with time were seen after exposure to the HNC were observed. Liquid acetone, toluene, and *n*-hexane present broad NMR signals that are shifted to lower frequency; these peaks are assigned to in-pore adsorbed VOCs where the shift is attributable to the ring currents arising from the graphene-like sheets. In addition, narrow signals at appear at the same chemical shift as those from the neat liquid VOCs. These latter peaks appear only at high loadings, consistent with pore saturation. In the case of acetone adsorption at high loadings, the adsorbate undergoes slow (~ 0.1 seconds) exchange between in-pore and ex-pore environments. Uptakes determined from $^1H$ NMR are obtained by calibrating the signal at various loadings, and are consistent with that of gas sorption analyzer data at saturation coverages, showing that NMR allows for fast determination of the ultimate adsorption capacities of VOCs within the hierarchical nanoporous carbons. Regarding gaseous adsorption, $^{1}H$ NMR spectra of vapor-adsorbed VOCs into HNC as a function of exposure time showed that VOCs occupy both mesopores and micropores, and by comparison to liquid adsorption, we proposed the data are consistent with an observation of Schroeder's Paradox. In the case of gas phase uptake of $CO_2$ we find that the HNC show high physisorption of $CO_2$ (4.3 mmol $g^{-1}$), consistent with potential application to carbon capture technologies. We conclude that the synthesis of hierarchical nanoporous carbons, and the NMR-determined pore distribution of adsorbates with loading and time, portends the observation of both new phenomena and novel technological applications in the multidisciplinary field of energy-environment-economics.

## Experimental Procedures

**Synthesis of hierarchical nanoporous carbons**. The pinewood chips were thoroughly washed and placed into a muffle furnace prior to carbonization. The carbonization temperature was 600 °C under a purified $N_2$ flow (0.5 L/min). After carbonization, the char was sieved to obtain particles of 1~2 mm in diameter. The char produced was mixed with $K_2CO_3$ with an impregnation $K_2CO_3$/char mass ratio of 3. The mixture was heated in a modified 2.45 GHz microwave oven with an output power of 700 W for 20 min, with humidified $N_2$ as the carrier gas. The resultant hierarchical nanoporous carbon was washed with 0.1 M hydrochloric acid and rinsed repeatedly with hot and cold distilled water to remove residual K from the surface of the sample until the filtrate reached neutral pH. The experimental setup is shown in **Figure 1a**. Additionally, to provide a comparison to the as-synthesized HNC, commercial activated carbons were obtained from EM industries Inc. Industries Inc. and characterized in tandem as described below.

**Sample characterization.** Scanning electron microscopy (SEM) images were acquired on a Hitachi S-2500 (Tokyo, Japan) analytical scanning electron microscope using a beam energy of 20 kV and an In-Lens detector. TEM images were acquired on a ThemIS microscope (TEM 0.5) at 300 kV. The specific surface area and pore structure of the samples were evaluated using a Micromeritics ASAP2010 physical adsorption instrument at 77 K in liquid $N_2$. The specific surface area was estimated by the Brunauer-Emmett-Teller method[25]. The pore size distribution for micropores was calculated using the t-plot method. Powder X-ray diffraction (PXRD) measurements were carried out on a Rigaku MiniFLex 6G Benchtop X-ray powder diffractometer operating at 20 mA and 40 kV using Cu $K\alpha_1$ radiation ($\lambda$ = 1.5406 Å) at room temperature.

**Preparation of samples in NMR rotors for adsorption experiment.** The schematic of preparation of samples was depicted in **Figure 3a.** The samples used herein were ground into powder (fine mesh) and placed into the vacuum oven at 120 °C overnight, then packed into 4 mm sealing cells, which were subsequently put into 4 mm outer diameter zirconia MAS rotors. Sealing cells were weighed prior to and after packing to determine the mass of the hierarchical nanoporous carbons. For liquid VOCs, a microsyringe was used to inject solvents (acetone (Sigma, 99 %), toluene (Sigma, 99.9 %), and *n*-hexane (Sigma, *n*-hexane 98.5 %)) into the sealing cell. The samples were subjected to NMR analysis 24 hours after adsorption in order to reach the adsorption equilibrium. The aforementioned above adsorption experiment was performed in the glove box with $N_2$ gas to avoid effects of moisture. The following mass balance equation was used to determine the used mass of VOCs injected into HNC:

$$W = \frac{W_2 - W_1}{W_1} \times 100\% \qquad (1)$$

where $W$ is the mass of VOCs normalized by the mass of the hierarchical nanoporous carbon material; $W_2$ is the weight of the HNC after adding VOCs; and $W_1$ is the weight of the HNC. Neat solvent experiments were performed on a mixture of KBr and pure VOCs in the sealing cell to ensure rotor stability during NMR. For gaseous adsorption, VOCs solvents and rotor with HNC were placed in separate scintillation vials, then placed in a sealed vial; further details are given below and in **Figure 3a**. Adsorption isotherms were measured by using the gas adsorption analyzer. After adsorption, the inserts with liquid/vapor VOC adsorbed HNC were transferred into the vacuum oven at 120 °C, left overnight, and then were stored in a desiccator for future use.

Prior to $CO_2$ adsorption, HNC samples were packed into a 3.2 mm rotor under nitrogen environment to avoid moisture. The rotor containing samples was then put into a home-bult gas set up[44] (**Figure 6b**). Before dosing $^{13}CO_2$ gas (Sigma-Aldrich, 99 atom % $^{13}C$, <3 atom % $^{18}O$), the samples were evacuated for 10 min. $^{13}CO_2$ dosing was carried out for overnight to reach the equilibration at room temperature (~298 K). Meanwhile, a gas gauge was used to control and record the pressure inside the samples. After adsorption, the rotor was sealed by the cap using a moveable plunger inside the set up to avoid air and moisture.

**NMR experiments.** The schematic of NMR experiments was shown in **Figure 3b.** The $^1H$ MAS NMR spectra were measured at 500.12 MHz (11.7 T) on a Bruker Avance spectrometer with a Bruker narrow bore H/C/N magic angle spinning (MAS) probe. The $^1H$ MAS one-pulse NMR spectra of VOCs adsorption in hierarchical nanoporous carbon was acquired at a sample spinning rate of 8 kHz. Neat VOCs with KBr were spun at 5 kHz. To eliminate the background signal from the NMR probe, both spin echo ($90^\circ-\tau-$¿$180^\circ-\tau-$¿ acquire) and one-pulse sequence measurements were used to record the $^{1}$H spectra[52]. A radio-frequency (RF) field strength ($B_1$) of 60 kHz and a spin echo delay of $\tau=$¿ 119 $\mu$s were used, while using a recycle delay of 1 s. $^{1}$H two-dimensional (2D) homonuclear exchange experiments were performed on samples with VOCs loadings where additional peaks (relative to the neat VOCs) emerged[53]. Mixing times in the range of 0.001 to 0.25 seconds were used. For $CO_2$ adsorption experiments, the NMR experiment was performed at 16.4 T using a Bruker 3.2 mm MAS probe with a MAS rate of 15 kHz. $^{13}$C NMR spectra by direct excitation was measured in the $CO_2$ adsorption experiment. The proton and $^{13}$C peaks of adamantane at 1.85 and 38.5 (tertiary carbon – left-hand resonance) ppm were used to as an external reference, respectively. All NMR experiments were performed at ambient temperature (~298 K). Spectral fitting was carried out using DMfit software. Deconvolutions were calculated using a mixture of Gaussian and Lorentzian lineshapes to describe the different features in the spectra.

The $^{1}$H MAS one-pulse NMR spectra of vapor VOCs adsorption in hierarchical nanoporous carbon were also acquired at a sample spinning rate of 8 kHz. The schematic of vapor adsorption in HNC is shown in **Figure S7**. HNC were packed into a 4 mm rotor in the $N_2$ glovebox. VOCs solvents and a rotor with HNC were placed in separate scintillation vials, then both placed in a parafilm-sealed beaker. To minimize moisture adsorption, this sealed beaker was placed in a glove box for various adsorption times.

After a specified adsorption time (e.g. 1 minute), the rotor was capped in the glove box and transferred to the NMR spectrometer.

To assess the diffusion of acetone within the mesopores of the HNC, vapor acetone was exposed to HNC for 1 minute in the sealed beaker, and then the rotor was quickly capped and placed in an Ar glove box for 3 h. Additional $^{1}H$ NMR experiments were carried out as shown in **Figure S7**. Prior to acetone vapor was exposed to HNC for 1 minute, argon gas was introduced to the glovebox and following by evacuating for 2 h. Afterwards, the rotor cap quickly inserted and sealed, and then the sample was heated to 55 ˚C for 30 min in the oven. After cooling to room temperature, a one-pulse MAS NMR experiment was performed.

**Adsorption isotherm experiments.** The adsorption isotherms were performed gravimetrically using a sorption analyzer (TA Instruments, model VTI-SA) at 298 K with $N_2$ as the carrier gas. The system recorded the equilibrium weight of the biomass based HNC in response to a step change in the concentration of the adsorbate (relative pressure range of 0.01~0.9). Between 3~5mg of HNC powder was weighed and placed into the container of the analyzer. Equilibrium was assumed to be reached when the weight changed by less than 0.001 % in a 5 min period.

**Acknowledgements**

This work was supported as part of the Center for Gas Separations Relevant to Clean Energy Technologies, an Energy Frontier Research Center funded by the U.S. This work was supported by the Department of Energy (DOE), Office of Basic Energy Sciences, Division of Materials Sciences and Engineering (contract no. DE-AC02-76SF00515). D.M.H. acknowledges support from the Joint Center for Energy Storage Research, an Energy Innovation Hub funded by the US Department of Energy, Office of Science, Basic Energy Science. We appreciate technical discussions with Dr. Alexander C. Forse and Dr. Thomas M. Osborn Popp.

**Author Contributions**

H.M., J.T., Y.C., and J.A.R conceived the idea and composed the manuscript. H.M. and J.T. planned the study, designed the experiment, analyzed the data. H.M. and J.T. performed all the experiments together with the assistance of J. X. performed the 2D exchange NMR experiment. Y.C. and J.A.R. supervised the project. All the authors reviewed and commented on the manuscript.

**Declaration of interests**

The authors declare no competing interests.

**Data availability**

The data that support the plots within this paper and other finding of this study are available from the corresponding authors on request.

**References**

1. Brüggemann, M., Hayeck, N. & George, C. (2018). Interfacial photochemistry at the ocean surface is a global source of organic vapors and aerosols. Nat. Commun. 9, 2101.

2. Boyd, P. G., Chidambaram, A., García-Díez, E., Ireland, C. P., Daff, T. D., Bounds, R., Gładysiak, A., Schouwink, P., et al. (2019). Data-driven design of metal–organic frameworks for wet flue gas $CO_2$ capture. Nature. 576, 253-256.

3. Chen, W. Y., Jiang, X., Lai, S., Peroulis, D. and Stanciu, L. (2020). Nanohybrids of a MXene and

transition metal dichalcogenide for selective detection of volatile organic compounds. Nat. Commun. 11, 1302.

4. Dong, J. and Zhang, K. (2017). Ultrathin two-dimensional porous organic nanosheets with molecular rotors for chemical sensing. Nat. Commun. 8, 1142.

5. Chen, W., Chen, S., Liang, T., Zhang, Q., Fan, Z.,Yin, H., Huang, K., Zhang, X., Lai, Z., and Sheng, P. (2018). High-flux water desalination with interfacial salt sieving effect in nanoporous carbon composite membranes. Nat. Nanotechnol. 13, 345–350.

6. McDonald, T. M., Mason, J. A., Kong, X., Bloch, E. D., Gygi, D., Dani, A., Crocella, V., Giordanino, F., Odoh, S. O., Drisdell, W.S. et al. (2015). Cooperative insertion of $CO_2$ in diamine-appended metal-organic frameworks. Nature. 519, 303–308.

7. Joo, W. J., Lee, J.H., Jang, Y., Kang, S.G., Kwon, Y.N., Chung J., Lee, S., Kim, C., Kim, T.H., Yang, C.W., et al. (2017). Realization of continuous Zachariasen carbon monolayer. Sci. Adv. 3, 1–9.

8. Yadavalli, T., Ames, J., Agelidis, A., Suryawanshi, R. & Jaishankar, D. (2019). Drug-encapsulated carbon (DECON): A novel platform for enhanced drug delivery. Sci. Adv. 1–13.

9. Xu, L., Li,Y., Gao, S., Niu, Y., Liu, H., Mei, C., J., Cai, Xu, C. (2020). Preparation and properties of cyanobacteria-based carbon quantum dots/polyvinyl alcohol/nanocellulose composite. Polymers (Basel). 12, 1–12.

10. Yu, D., Goh, K., Wang, H., Wei, L., Jiang, W., Zhang, Q., Dai, L., Chen, Y., (2014). Scalable synthesis of hierarchically structured carbon nanotube-graphene fibres for capacitive energy

storage. Nat. Nanotechnol. 9, 555–562.

11. Tseng, P., Napier, B., Zhao, S., Mitropoulos, A.N., Applegate, M. B., Marelli, B., Kaplan, D. L., Omenetto, F. G. (2017). Directed assembly of bio-inspired hierarchical materials with controlled nanofibrillar architectures. Nat. Nanotechnol. 12, 474–480.

12. Abraham, J., Vasu, K. S., Williams, C. D., Gopinadhan, K., Su, Y., T. C., Cherian, J. Dix, Prestat, E., Haigh, S. J., Grigorieva, I. V., Carbone, P. (2017). Tunable sieving of ions using graphene oxide membranes. Nat. Nanotechnol. 12, 546–550.

13. Wu, J., Wu, J., Xu, F., Li, S., Ma, P., Zhang, X., Liu, Q., Fu, R., and Wu, D. (2019). Porous polymers as multifunctional material platforms toward task-specific applications. Adv. Mater. 31, 1–45.

14. Wang, H., Min, S., Ma, C., Liu, Z., Zhang, W., Wang, Q., Li, D., Li, Y., Turner, S., Han, Y., et al. (2017). Synthesis of single-crystal-like nanoporous carbon membranes and their application in overall water splitting. Nat. Commun. 8, 13592.

15. Jessen, B. S., Gammelgaard, L., Thomsen, M. R., Mackenzie, D. M. A., Thomsen, J. D., Caridad, J. M., Duegaard, E., Watanabe, K., Taniguchi, T., and Booth, T. J., et al. (2019). Lithographic band structure engineering of graphene. Nat. Nanotechnol. 14.

16. Xia, H., Tang, H., Zhou, B., Y., Li, X., Zhang, Shi, Z., Deng, L., Song, R., Li, L., Zhang, Z., and Zhou, J. (2020). Mediator-free electron-transfer on patternable hierarchical meso/macro porous bienzyme interface for highly-sensitive sweat glucose and surface electromyography monitoring. Sensors Actuators, B Chem. 312, 12792.

17. Lin, X. , Liang, Y., Lu, Z., Lou, H., Zhang, X., Liu, S., Zheng, B., Liu, R., Fu, R., and Wu D. (2017). Mechanochemistry: A green, activation-free and top-down strategy to high-surface-area carbon materials. ACS Sustain. Chem. Eng. 5, 8535–8540.

18. Du, Y., Huang, Z., Wu, S., K., Xiong, X., Zhang, Zheng, B., Nadimicherla, R., Fu, R., and Wu, D. (2018). Preparation of versatile yolk-shell nanoparticles with a precious metal yolk and a microporous polymer shell for high-performance catalysts and antibacterial agents. Polymer. 137, 195–200.

19. Zheng, X., Shen, G., Wang, C., Li, Y., Dunphy, D., Hasan, T., Brinker, C. J., and Su, B., (2017). Bio-inspired Murray materials for mass transfer and activity. Nat. Commun. 8, 14921.

20. Wang, X., Wang, X., Huang, Z., D., Miao, D., Miao, J., Zhao, J., Yu, and Ding, B. (2018). Biomimetic fibrous Murray membranes with ultrafast water transport and evaporation for smart moisture-wicking fabrics. ACS Nano. 13, 1060–1070.

21. Adinata, D., Wan Daud, W. M. A. & Aroua, M. K. (2007). Preparation and characterization of activated carbon from palm shell by chemical activation with $K_2CO_3$. Bioresour. Technol. 98, 145–149.

22. Dahal, N., García, S., Zhou, J. & Humphrey, S. M. (2012). Beneficial effects of microwave-assisted heating versus conventional heating in noble metal nanoparticle synthesis. ACS Nano 6, 9433–9446.

23. Wang, H. et al. (2012). Adsorption and desorption of mixtures of organic vapors on beaded activated carbon. Environ. Sci. Technol. 46, 8341–8350.

24. Lashaki, M. J. et al. (2012). Effect of adsorption and regeneration temperature on irreversible adsorption of organic vapors on beaded activated carbon. Environ. Sci. Technol. 46, 4083–4090.

25. Brunauer, S., Emmett, P. H. & Teller, E. (1938). Adsorption of gases in multimolecular layers. J. Am. Chem. Soc. 60, 309–319.

26. Jahandar Lashaki, M. et al. (2016). The role of beaded activated carbon's surface oxygen groups on irreversible adsorption of organic vapors. J. Hazard. Mater. 317, 284–294.

27. Pel, L., Valckenborg, R. M. E., Kopinga, K., Aarden, F. B. & Kerkhof, P. J. A. M. (2003). Nitrobenzene adsorption in activated carbon as observed by NMR. AIChE J. 49, 232–236.

28. Carter, G. T. et al. (2013). Mapping of functional groups in metal-organic frameworks. Science. 341, 882–886.

29. Forse, A. C., Merlet, C., Allan, P. K., Humphreys, E. K., Griffin, J. M., Aslan, M., Zeiger, M., Presser, V., Gogotsi, Y., and C. P., Grey. (2015). New insights into the structure of nanoporous carbons from NMR, Raman, and pair distribution function analysis. Chem. Mater. 27, 6848–6857.

30. Deschamps, M., Gilbert, E., Azais, P., Raymundo-Piñero, E., Ammar, M. R., Simon, P., Massiot, D.,and Béguin, F. (2013). Exploring electrolyte organization in supercapacitor electrodes with solid-state NMR. Nat. Mater. 12, 351–358.

31. Hippauf, F., Fulik, N., Hippauf, F., Leistenschneider, D., Paasch, S., Kaskel, S., Brunner, E., and Borchardt, L. (2018). Electrolyte mobility in supercapacitor electrodes – solid state NMR studies on hierarchical and narrow pore sized carbons. Energy Storage Mater. 12, 183–190.

32. Schroeder, P. (1903). Uber Erstarrungs–und Quellungserscheinungen von Gela-tine. Z. Phys.

Chem. 45, 57.

33. Román, S., Ledesma, B., Sabio, E., González, J. F. & González, C. M. (2016). Production of cost-effective mesoporous materials from prawn shell hydrocarbonization. Nanoscale Res. Lett. 11, 435.

34. Sun, Y., Wei, J., Wang, Y. S., Yang, G. & Zhang, J. P. (2010). Production of activated carbon by $K_2CO_3$ activation treatment of cornstalk lignin and its performance in removing phenol and subsequent bioregeneration. Environ. Technol. 31, 53–61.

35. Chen, R., Li, L., Liu, Z., Liu, M., Wang C., Li, H., Ma, W., and Wang, S. (2017). Preparation and characterization of activated carbons from tobacco stem by chemical activation. J. Air Waste Manag. Assoc. 67, 713–724.

36. Horvath, G. and Kawazoe, K. (1983). Method for calclualtion effective pore size distribution in molecular sieve carbon. J. Chem. Eng. Japan 16, 470.

37. Carrott, P. J. M., Carrott, M. M. L. R., Mourão, P. A. M. & Lima, R. P. (2004). Preparation of activated carbons from cork by physical activation in carbon dioxide. Adsorpt. Sci. Technol. 21, 669–681.

38. Foo, K. Y. & Hameed, B. H. (2012). Mesoporous activated carbon from wood sawdust by $K_2CO_3$ activation using microwave heating. Bioresour. Technol. 111, 425–432.

39. Forse, A. C., Griffin, J. M., Merlet, C., Carretero-Gonzalez, J., Raji, A. R. O., Trease, N. M. and Grey, C. P. (2017). Direct observation of ion dynamics in supercapacitor electrodes using in situ diffusion NMR spectroscopy. Nat. Energy 2, 16216.

40. Harris, R. K., Thompson, T. V., Norman, P. R. and Pottage, C. (1996). Adsorption competition

onto activated carbon, studied by magic-angle spinning NMR. J. Chem. Soc. - Faraday Trans. 92, 2615–2618.

41. Harris, R. K., Thompson, T. V., Norman, P. R. & Pottage, C. (1999). Phosphorus-31 NMR studies of adsorption onto activated carbon. Carbon N. Y. 37, 1425–1430.

42. Devautour-vinot, S., Maurin, G., Serre, C., Horcajada, P., Cunha, D. P., Guillerm, V., Costa, E. S., Taulelle, F., and Martineau C. (2012). Structure and dynamics of the functionalized MOF type UiO-66(Zr): NMR and dielectric relaxation spectroscopies coupled with DFT calculations. Chem. Mater. 24, 2168–2177.

43. Anderson, R. J., McNicholas, T. P., Kleinhammes, A., Wang, A., Liu J., and Wu Y. (2010). NMR Methods for characterizing the pore structures and hydrogen storage properties of microporous carbons. J. Am. Chem. Soc. 132, 8618–8626.

44. Forse, A. C., Milner, P. J., Lee, J. H., Redfearn, H. N., Oktawiec, J., Siegelman, R. L., Martell, J. D., Dinakar., L. B., Porter-Zasada, Gonzalez, M. I., et. al. (2018). Elucidating $CO_2$ chemisorption in diamine-appended metal-organic frameworks. J. Am. Chem. Soc. 140, 18016–18031.

45. Valiollahi, S., Kavianpour, B., Raeissi, S. & Moshfeghian, M. (2016). A new Peng-Robinson modification to enhance dew point estimations of natural gases. J. Nat. Gas Sci. Eng. 34, 1137–1147.

46. Ania, C. O., Cabal, B., Parra, J. B., Arenillas, A., Arias, B., and Pis, J. J. (2008). Naphthalene adsorption on activated carbons using solvents of different polarity. Adsorption 14, 343–355.

47. Vallieres, C., Winkelmann, D., Roizard., D., Favre, E., Scharfer, P., Kind, M., (2006). On

Schroeder's paradox. J. Memb. Sci. 278, 357–364.

48. Beers, K. M., Yakovlev, S., Jackson, A., Wang, X., Hexemer, A., Downing, K. H., and Balsara, N.P. (2014). Absence of Schroeder's paradox in a nanostructured block copolymer electrolyte membrane. J. Phys. Chem. B 118, 6785–6791.

49. Liu, X., Sun, C., Liu., H, Tan., W., Wang, W., Snape, C. (2019). Developing hierarchically ultra-micro/mesoporous biocarbons for highly selective carbon dioxide adsorption. Chem. Eng. J. 361, 199–208.

50. Millward, A. R. and Yaghi, O. M. (2005). Metal-organic frameworks with exceptionally high capacity for storage of carbon dioxide at room temperature. J. Am. Chem. Soc. 127, 17998–17999.

51. Forse, A. C., Griffin, J. M., Presser, V., Gogotsi, Y. and Grey, C. P. (2014). Ring current effects: Factors affecting the NMR chemical shift of molecules adsorbed on porous carbons. J. Phys. Chem. C. 118, 7508–7514.

52. Nandy, A., Forse, A. C., Witherspoon, V. J. and Reimer, J. A. (2018). NMR spectroscopy reveals adsorbate binding sites in the metal-organic framework UiO-66(Zr). J. Phys. Chem. C. 122, 8295–8305.

53. Aue, W. P., Bartholdi, E. and Ernst, R. R. (1976). Two-dimensional spectroscopy. Application to nuclear magnetic resonance. J. Chem. Phys. 64, 2229–2246.

## Figures and Captions

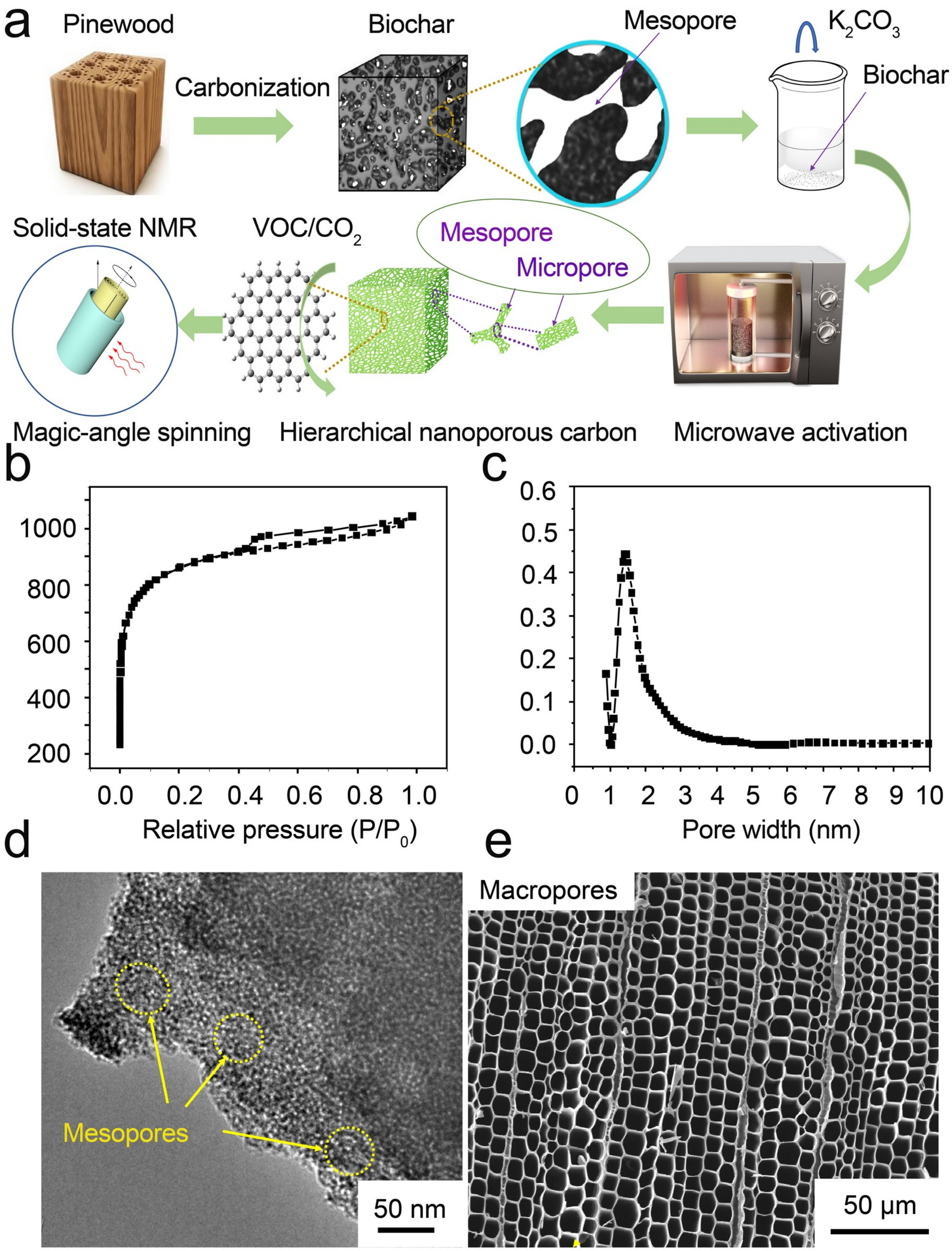

**Figure 1 | Preparation and physical characterization of HNC. a,** Schematic diagram of the fabrication process and characterization of the HNC; **b.** Ar adsorption isotherm at 77 K and **c.** pore size distribution of biochar and HNC; **d, and e,** TEM and SEM images of the HNC framework.

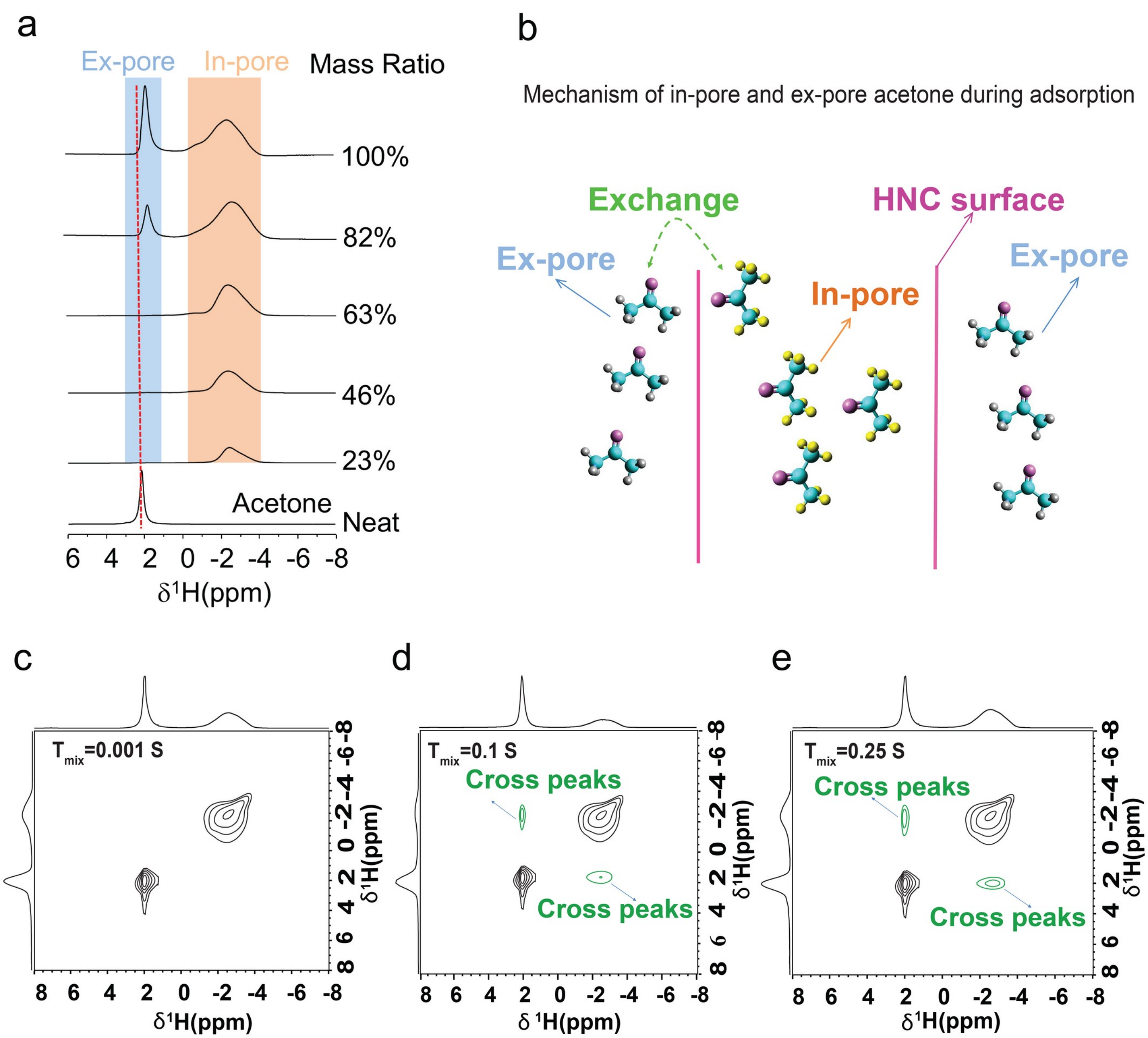


**Figure 2 | Adsorption of liquid acetone in HNC by NMR. a,** $^1$H NMR spectra of acetone adsorbed onto HNC as a function of loading. The mass ratio is the (mass of acetone used/mass of hierarchical porous nanocarbon material). **b,** Scheme of the local environments of acetone molecules in HNC, including in-pore, ex-pore and exchange species; **c, d, and e,** 2D $^1$H homonuclear correlation experiments. Experiments were performed on a sample with 100% mass ratio of (acetone/HNC), with mixing times of

0.001, 0.1 and 0.25 seconds, respectively. The cross peaks appearing at mixing times of 0.1 and 0.25 s demonstrating slow exchange between in-pore and ex-pore environments.

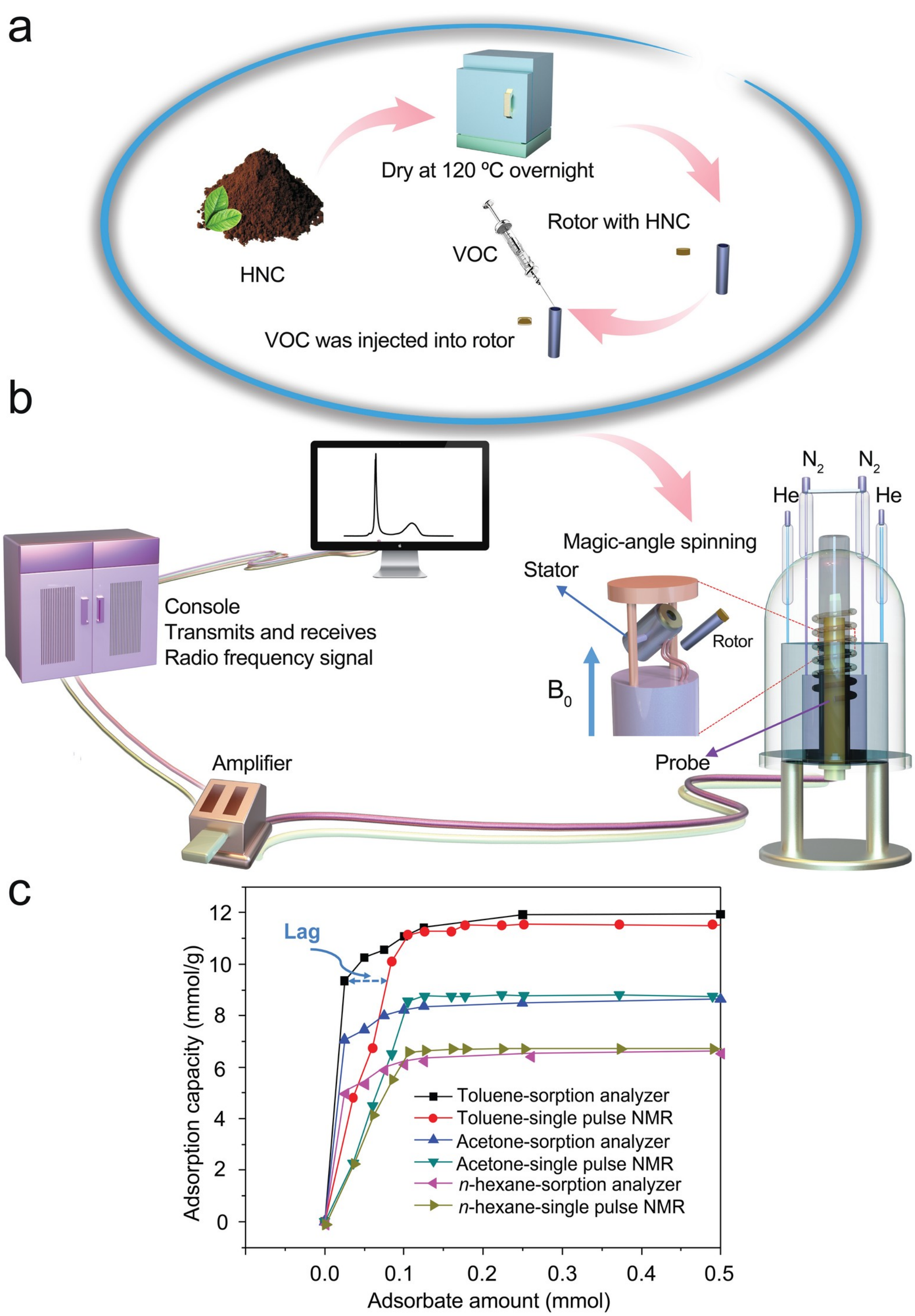

**Figure 3 | Uptakes of NMR and gas sorption data. a,** Schematic of the liquid VOC adsorption process; **b,** Schematic of the solid-state NMR measurements of liquid VOC loaded HNC; **c,** Comparison of uptakes between NMR data and gas sorption analyzer data for acetone, toluene and *n*-hexane loaded hierarchical nanoporous carbon at room temperature (~298 K). NMR data corroborate the ultimate adsorption capacity, but lag the isotherm data at low loadings.

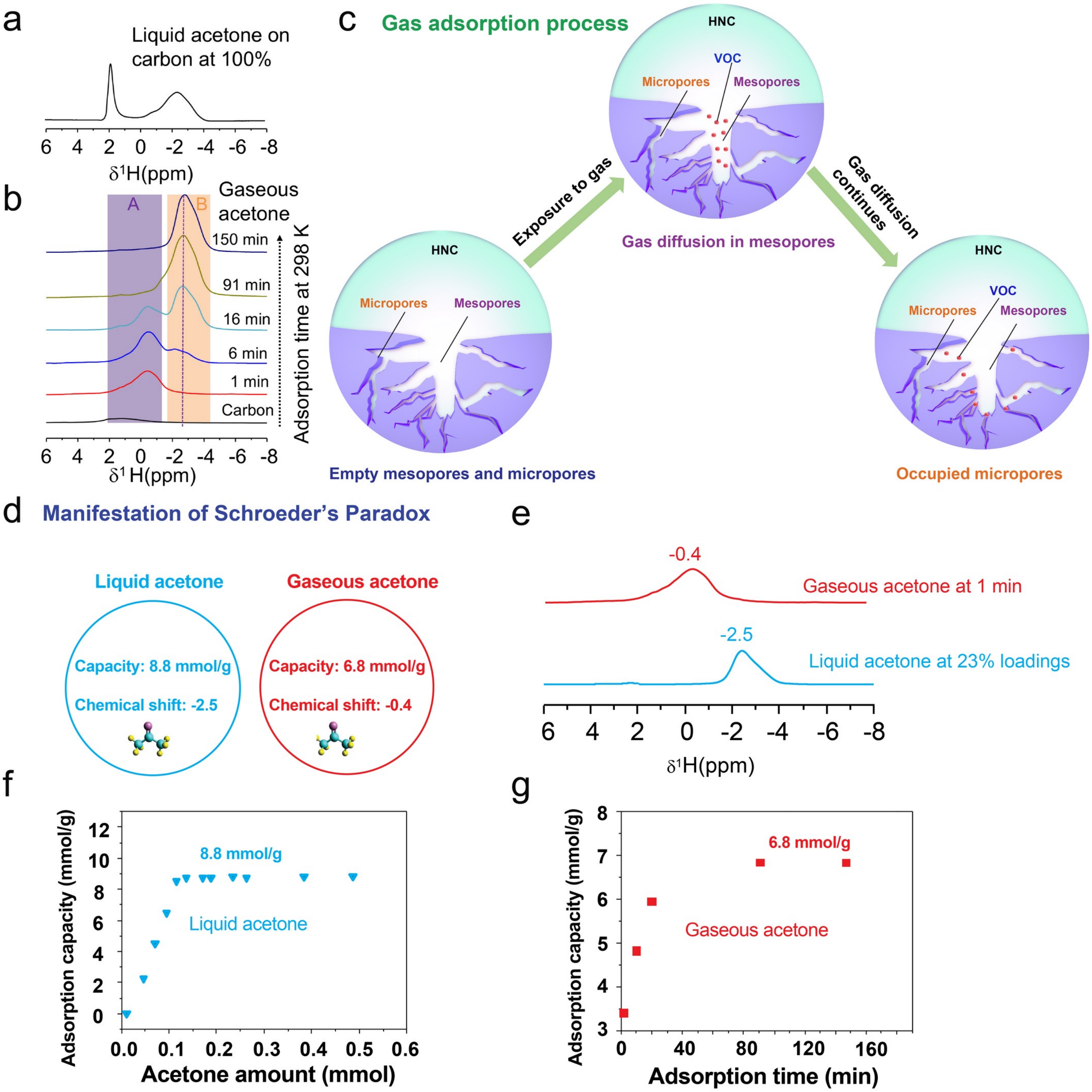


**Figure 4 | Vapor acetone adsorption mechanism and manifestation of Schroeder's Paradox onto HNC. a,** $^{1}$H NMR spectra of liquid acetone at 100 wt % loading is shown as a comparison; **b,** $^{1}$H NMR spectra of vapor acetone subject to HNC as a function of adsorption time at ~298K; **c,** Mechanism of vapor acetone adsorption process in different pores; **d ~ e,** Manifestation of Schroeder's Paradox on liquid and gaseous acetone adsorption capacity and chemical shift in HNC; **e,** Difference in chemical shifts; **f and g,** Difference in adsorption capacities; **(f,** The liquid acetone adsorption capacity at 100 wt %; **g,** The adsorption capacity ("A"+"B") changes with increase of adsorption time, and it reaches saturation over 91 min.)

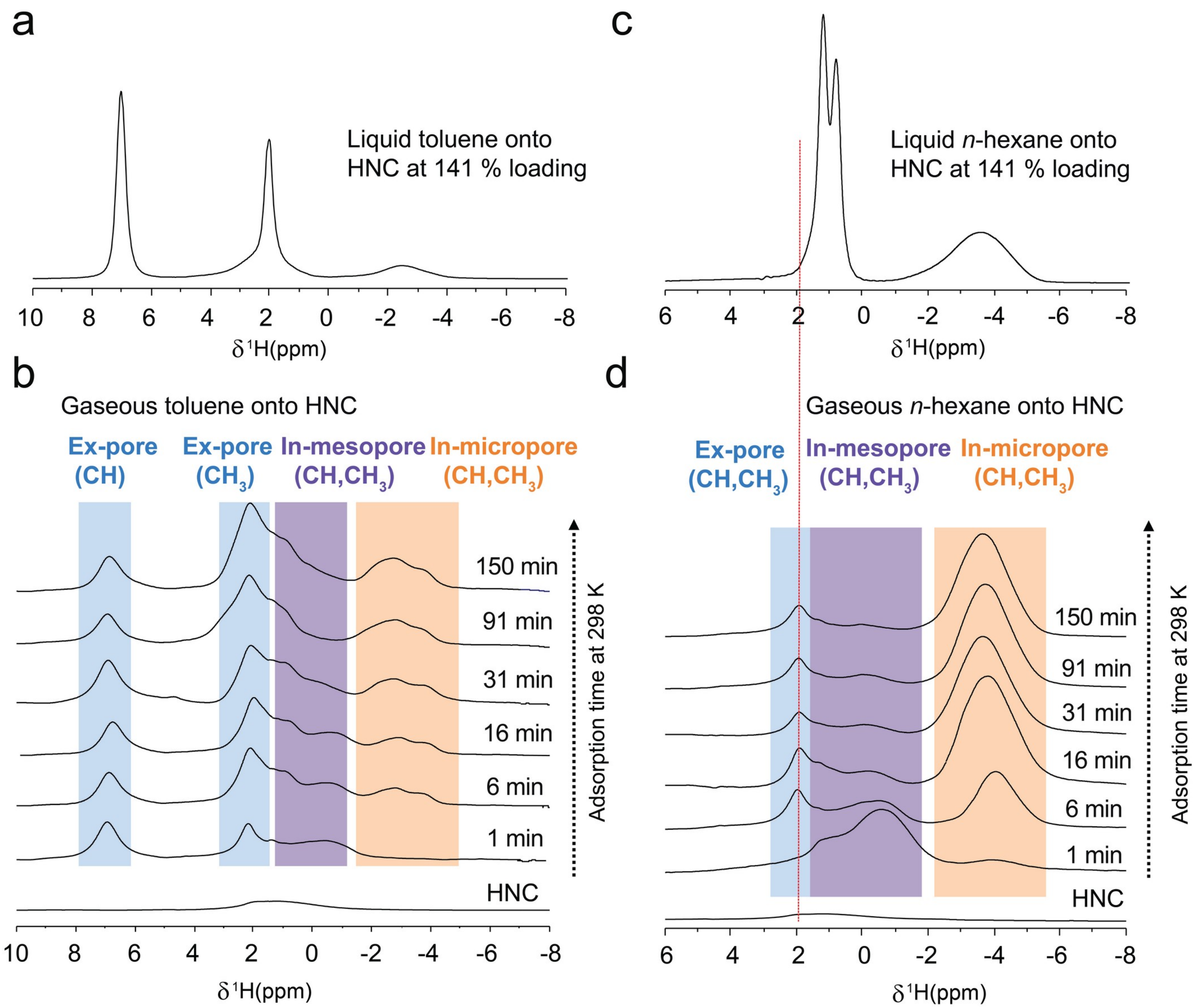


**Figure 5 | Vapor toluene and *n*-hexane adsorption on hierarchical nanoporous carbon. a,** $^1H$ NMR spectra of liquid toluene at 141 wt % loading is shown as a comparison; **c,** $^1H$ NMR spectra of liquid *n*-hexane at 141 wt % loading is shown as a comparison; **b,** $^1H$ NMR spectra of vapor toluene subject to HNC as a function of adsorption time**; d,** $^1H$ NMR spectra of vapor *n*-hexane subject to HNC as a function of adsorption time.

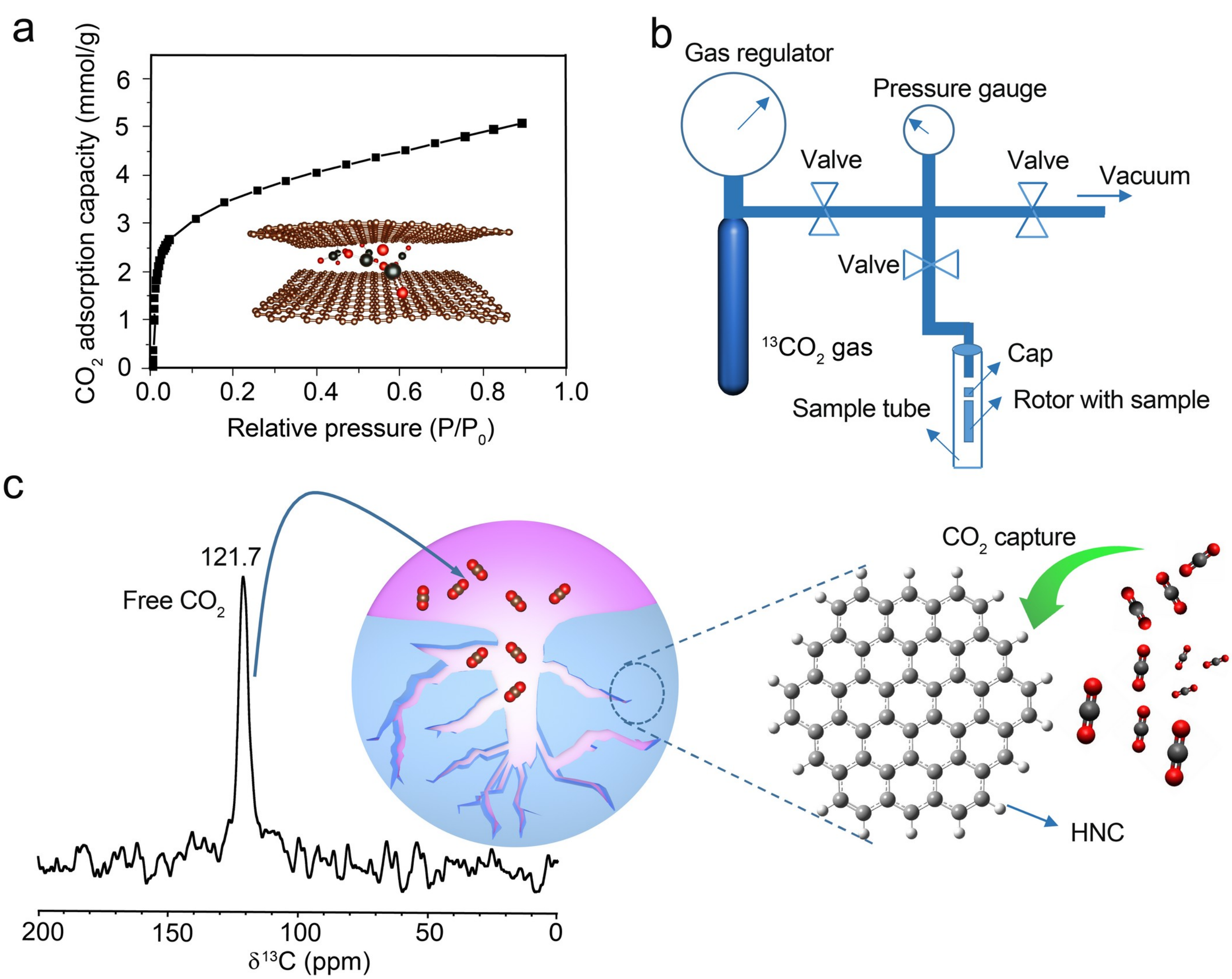


**Figure 6 | $CO_2$ adsorption on hierarchical nanoporous carbon. a,** $CO_2$ adsorption isotherm onto HNC at 298 K and 1 bar; adsorption isotherm samples were activated under $N_2$ at 120 °C for 2 h, followed by activation under vacuum at 120 °C for 4 h; **b,** Schematic of set up for $CO_2$ gas dosing into NMR samples; **c,** $^{13}C$ NMR spectra by direct excitation (no $^1H$ decoupling) on $^{13}CO_2$ loaded HNC at 755 mbar.